

Verification of continuous variable entanglement with undetected photons

Sanjukta Kundu,^{1,*} Balakrishnan Viswanathan,^{2,3,*} Paweł Szczypkowski,¹
Gabriela Barreto Lemos,⁴ Mayukh Lahiri,^{2,†} and Radek Lapkiewicz^{1,‡}

¹*Institute of Experimental Physics, University of Warsaw. Pasterura 5 Warsaw*

²*Department of Physics, Oklahoma State University,
145 Physical Sciences Bldg, Stillwater, Oklahoma 74078*

³*Current address: Optics and Quantum Information Group, The Institute of Mathematical Sciences,
CIT Campus, Chennai 600113, India*

⁴*Instituto de Física, Universidade Federal do Rio de Janeiro,
Av. Athos da Silveira Ramos, Rio de Janeiro, CP: 68528, Brazil*

(Dated: January 14, 2026)

We verify transverse spatial entanglement of photon-pairs generated in spontaneous parametric down conversion using a nonlinear interferometric technique without relying on any coincidence detection. We experimentally demonstrate the violation of the Einstein-Podolsky-Rosen criterion and of the Mancini-Giovannetti-Vitali-Tombesi criterion using single photon interference of one of the photons of the pairs. We also provide a comprehensive theoretical analysis. The experimental results that we have obtained show good agreement with the theoretical values. Our method performs well under experimental losses and can be applied to highly non-degenerate sources, where there are no suitable detectors for one of the photons in the quantum state and our method could also be extended to the discrete degrees of freedom to certify high-dimensional (OAM) entanglement.

I. INTRODUCTION

Entanglement lies at the foundation of quantum mechanics and serves as a central resource across modern quantum technologies, enabling advances in imaging, communication, computation, and metrology. In continuous-variable photonic systems, spatial entanglement in position and momentum (see [1] and references therein) provides access to high-dimensional Hilbert spaces and enhanced information-encoding capabilities. These transverse spatial correlations have opened opportunities across various quantum technologies, including quantum imaging [2], quantum metrology [3, 4], and quantum key distribution [5]. However, conventional methods for verifying such correlations rely on coincidence detection of both photons in a pair [6–9], which can be experimentally challenging, particularly for highly non-degenerate sources where efficient detectors may not exist for one of the photons. This limitation motivates us the development of alternative strategies for certifying continuous-variable entanglement that do not depend on coincidence measurements and remain robust under realistic experimental imperfections.

In contrast to the traditional approach of characterizing entanglement in any two-photon system, which relies on detection of both photons via coincidence measurement (Fig. 1a) [10–14], we take an interferometric approach (Fig. 1b) that dispenses with the use of coincidence detection. Our method relies on a phenomenon often called *induced coherence without induced emission*

[15, 16]. Techniques based on this phenomenon have recently been applied to measure entanglement in two-qubit photonic systems without detecting one of the photons [17–20]. Here, we demonstrate both theoretically and experimentally that it is possible to characterize spatial (momentum-position) entanglement in a bipartite photonic system using only single-photon counting rate without any postselection.

Our method provides practical advantage over traditional techniques when one of the two photons lies in a spectral range for which adequate detectors are not available. Moreover, it performs well even under high experimental losses. The method can also be implemented without using single-photon detectors, i.e., using standard cameras, such as CCD or sCMOS.

The paper is organized as follows: In Sec. II, we outline the principle of our method. In Sec. III, we describe the experiment in detail followed by a rigorous discussion of the underlying theory in Sec. IV. The results are presented in Sec. V and Sec. VI provides a brief discussion of our method. We finally summarize our work in Sec. VII.

II. PRINCIPLE

Let us consider a photon pair that can be correlated in momentum and position. The two photons constituting a pair will be called signal (S) and idler (I). We represent the transverse momenta of signal and idler photons at the source plane by $\hbar\mathbf{k}_S$ and $\hbar\mathbf{k}_I$, respectively, where $\mathbf{k}_S \equiv (k_{Sx}, k_{Sy})$ and $\mathbf{k}_I \equiv (k_{Ix}, k_{Iy})$. Likewise, the transverse positions of signal and idler photons at the source are denoted by $\rho_S \equiv (x_S, y_S)$ and $\rho_I \equiv (x_I, y_I)$, respectively. The photon pair is en-

* These authors contributed equally to this work.

† mlahiri@okstate.edu

‡ radek.lapkiewicz@fuw.edu.pl

tangled in position-momentum if the following Einstein-Podolsky-Rosen (EPR) type criterion is violated [6, 21–23]

$$\Delta^2(\rho_I|\rho_S) \Delta^2(\mathbf{k}_I|\mathbf{k}_S) > \frac{1}{4}, \quad (1)$$

where $\Delta^2(\xi_I|\xi_S)$ is the *conditional variance*, representing uncertainty in the measurement of variable ξ_I , conditional on the measurement of variable ξ_S .

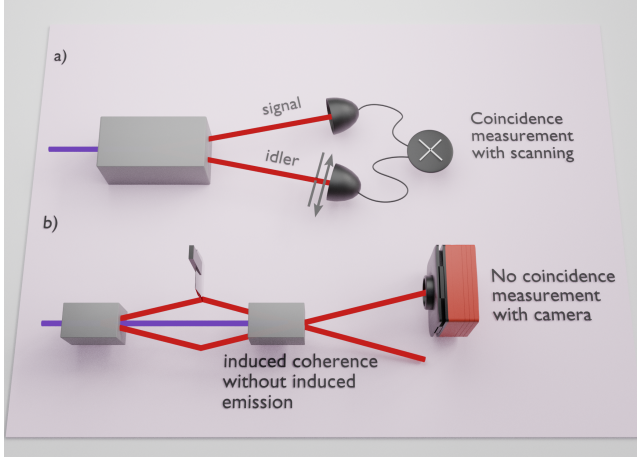


FIG. 1. Comparison between the principle of standard coincidence-based entanglement measurement and our method using induced coherence. (a) Standard approach: Spatial entanglement of photon pairs generated via SPDC is typically measured by detecting both signal and idler photons in coincidence. Scanning detectors are usually used to record joint probability distributions in position or momentum bases. (b) Our approach: Using an induced coherence interferometer, only the signal photon is detected on an EM-CCD camera, while the idler photon remains undetected. By analyzing the interferometric image of the knife-edge in position and momentum space, we retrieve the same conditional variances without coincidence detection.

Measuring $\Delta^2(\rho_I|\rho_S)$ and $\Delta^2(\mathbf{k}_I|\mathbf{k}_S)$ is the cornerstone of testing this criterion. We realize these measurements by analyzing the single-photon interference pattern generated by *induced coherence without induced emission* [15, 16]. We now consider two mutually coherent twin-photon sources, each of which can generate the target quantum state. These can be at two spatially separated locations, for example, two nonlinear crystals pumped by two mutually coherent laser beams (Fig. 1b). These two sources can also be at the same location [24], for example, in a single nonlinear crystal pumped from two directions by two mutually coherent laser beams (Figs. 2a and 2b). For simplicity of discussion, we choose the former arrangement to describe the principle. For compactness and the stability of the interferometer, the latter approach is taken in the experiment. The same theoretical treatment is applicable to both scenarios.

The paths of the photon pair generated by individual sources are perfectly aligned (Fig. 1b), such that it is im-

possible to determine the “which-way information” corresponding to a detected photon [15, 16, 24], resulting in a single-photon interference pattern. When we place an object in the path of the undetected photon between the two sources, the spatial information of the object appears in the interference pattern [25–28]. We show that if the object is known, one can determine the conditional variances, $\Delta^2(\rho_I|\rho_S)$ and $\Delta^2(\mathbf{k}_I|\mathbf{k}_S)$, from the single-photon interference data. Furthermore, the same data allow us to test the violation of the Mancini-Giovannetti-Vitali-Tombesi (MGVT) criterion [29], whose relevant form in our case is

$$\Delta^2 \mathbf{K}_+ \Delta^2 \rho_- \geq 1, \quad (2)$$

where $\Delta^2 \mathbf{K}_+ \equiv (\Delta^2 K_{x+}, \Delta^2 K_{y+})$ and $\Delta^2 \rho_- \equiv (\Delta^2 X_-, \Delta^2 Y_-)$ are the variances of $\mathbf{K}_+ = \mathbf{k}_I + \mathbf{k}_S$ and $\rho_- = \rho_S - \rho_I$, respectively.

III. DESCRIPTION OF THE EXPERIMENT

Toward certifying the position-momentum entanglement experimentally with our method, we build a double-pass non-linear interferometer using the collinear type-II spontaneous parametric down-conversion (SPDC) process (Figs. 2a and 2b). Our interferometer is based on the frustrated two-photon creation interferometer [24]. We pump a 2 mm long (L) periodically poled potassium titanyl phosphate (ppKTP) nonlinear crystal maintained at 32°C with 405 nm (λ_p) laser. The pump is focused on the crystal with a waist of 108 μm (w_0) and it results in the creation of degenerate, orthogonally polarized twin-photon pairs (signal and idler) at a wavelength 810 nm into paths S_1 and I_1 . We separate the pump beam from the twin-photon pair with a dichroic mirror. Sequentially, we employ a polarizing beam splitter to separate the signal from the idler. The pump, signal, and idler are directed along three distinct paths and are reflected back by mirrors M_1 , M_2 , and M_3 , respectively, placed at the end of the three interferometric arms. After getting reflected back from the mirrors, both signal and idler photons and the pump pass through the crystal. The back-propagating pump beam can generate the second set of twin-photon pairs (signal and idler) into paths S_2 and I_2 . Thus, the two-possible ways (forward and backward) of creating photon pairs can interfere. It is important to ensure that the photon paths (S_1, I_1) corresponding to the first pass of the pump beam are aligned precisely, and overlap with the photon paths (S_2, I_2) corresponding to the second pump pass. We use a short-pass dichroic mirror to separate the signal and idler photons from the pump beam and direct them toward an EM-CCD camera. Once we assure that the alternative paths overlap and that the photon pairs, emitted as the pump passes through the crystal twice, are indistinguishable, we observe the interference of either the signal or idler photons.

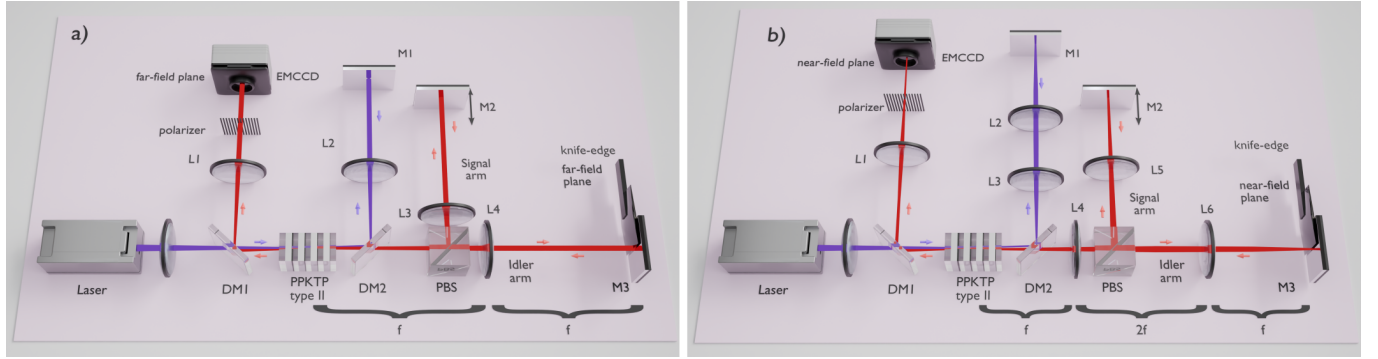


FIG. 2. Experimental setup for measuring the edge-spread function (ESF) in (a) momentum space and (b) position space. A 405 nm pump beam generates degenerate, orthogonally polarized photon pairs via type-II SPDC in a ppKTP crystal. Interference of the generated photon is enabled by induced coherence. A knife edge is placed in the idler arm to perform edge measurements in either the far-field (a) or near-field (b) of the crystal.

(a) Momentum-space configuration: All lenses used have 200 mm focal lengths. The pump is focused onto the crystal, generating SPDC photon pairs. DM2 separates the forward-propagating pump from the signal and idler photons. Lens L2 projects the crystal's far-field onto mirror M1 and simultaneously focuses the back-propagating pump (reflected from M1) into the crystal. After the PBS, lenses L3 (signal arm) and L4 (idler arm) project the far-field onto mirrors M2 and M3, respectively. The knife edge is placed just before M3 in the idler arm, in the far-field plane of the crystal. The back-propagating signal and idler are separated from the pump by DM1, and lens L1 images the crystal's far-field onto the EMCCD camera. A polarizer selects the signal photon polarization before detection.

(b) Position-space configuration: All lenses have 100 mm focal lengths. The pump is focused onto the crystal, where SPDC photon pairs are generated. DM2 separates the forward-propagating pump from the down-converted photons. Lenses L3 and L4 image the crystal's near-field onto M1 and simultaneously focus the back-propagating pump (from M1) into the crystal. Additional 4f imaging systems (L4–L5 for the signal arm and L4–L6 for the idler arm) project the near-field onto mirrors M2 and M3. The signal and idler photons are separated by a PBS placed after L4. The knife edge is positioned just before M3 in the near-field plane of the crystal. The back-propagating signal and idler are separated from the pump at DM1, and a 2f–2f imaging system using L1 maps the crystal's near-field onto the EMCCD camera. A polarizer selects the detected signal photon.

We place a knife-edge in front of the mirror M_3 in such a way that a part of the idler beam is blocked. An image of the knife-edge appears in the visibility of the interference pattern (Fig. 3a). This image can be interpreted as an edge-spread function. For the verification of position-momentum entanglement, we measure the corresponding edge-spread function in both momentum space (Fig. 2a) and position space (Fig. 2b), respectively (see Eqs. (13a) and (13b) in Sec. IV below and Fig. 4 in Sec. V below). We access these two Fourier conjugate spaces (momentum and position correlations of signal and idler photons) with appropriate lens systems.

In the momentum correlation measurement (Fig. 2a), we place a single lens of focal length $f = 200$ mm in each arm of our interferometer. Here, the object (in our case, the knife-edge) and the camera are placed in the far field (Fourier plane) of the nonlinear crystal. The idler photons (I_1, I_2), generated during either the forward or backward pass are blocked and remain undetected by using a proper orientation of a polarizer placed in front of the EMCCD camera, permitting only signal photons (S_1, S_2) to pass through.

To measure the position correlation of the twin-photon pair (Fig. 2b), we use a 4f-imaging system, in every arm of our interferometer, consisting of a pair of lenses of focal lengths of $f = 100$ mm such that both the knife-edge and the mirrors are in the near field (image plane)

of the crystal with unit magnification [30, 31].

IV. THEORY

We present a detailed theoretical analysis assuming that the two photons can have different wavelengths, i.e., the photon-generating process creates a non-degenerate energy spectrum. The degenerate case can be readily obtained by setting the wavelengths of the two photons equal in the resulting formulas. Throughout the analysis, we assume that photons propagate as paraxial beams and are incident normally on both the object and the detector. Our analysis is based on the theory developed through Refs. [26, 27, 32].

In the setup (Figs. 2a and 2b), a single nonlinear crystal is weakly pumped from two opposite directions by two mutually coherent laser beams. The first pass of the pump (from left in Figs. 2) through the nonlinear crystal is equivalent to the source on the left in Fig. 1b. Likewise, the second pass of the pump (from right in Figs. 2) through the nonlinear crystal is equivalent to the source on the right in Fig. 1b. We denote the first and second passes of the pump by Q_1 and Q_2 , respectively.

The twin-photon state generated by an individual pass (j) of the pump through nonlinear crystal can be ex-

pressed as

$$|\psi_j\rangle = \int d\mathbf{k}_S d\mathbf{k}_I C(\mathbf{k}_S, \mathbf{k}_I) |\mathbf{k}_S\rangle_{S_j} |\mathbf{k}_I\rangle_{I_j}, \quad (3)$$

where $j = 1, 2$ ket $|\mathbf{k}_S\rangle_{S_j}$ ($|\mathbf{k}_I\rangle_{I_j}$) represents a signal (idler) photon with momentum $\hbar\mathbf{k}_S$ ($\hbar\mathbf{k}_I$) emitted by Q_j , and $C(\mathbf{k}_S, \mathbf{k}_I)$ is the two-photon amplitude. The momentum correlation between the two photons is fully characterized by the joint probability density

$$P(\mathbf{k}_S, \mathbf{k}_I) = |C(\mathbf{k}_S, \mathbf{k}_I)|^2, \quad (4)$$

and the position correlation is fully characterized by the joint probability density

$$P(\boldsymbol{\rho}_S, \boldsymbol{\rho}_I) = \left| \frac{1}{4\pi^2} \int d\mathbf{k}_S d\mathbf{k}_I C(\mathbf{k}_S, \mathbf{k}_I) e^{i(\mathbf{k}_S \cdot \boldsymbol{\rho}_S + \mathbf{k}_I \cdot \boldsymbol{\rho}_I)} \right|^2. \quad (5)$$

These two probability densities are assumed to take the following Gaussian forms (cf. [1]; see also Appendix A)

$$P(\mathbf{k}_I, \mathbf{k}_S) \propto \exp \left[-\frac{\sigma_+^2}{2} |\mathbf{k}_I + \mathbf{k}_S|^2 \right], \quad (6a)$$

$$P(\boldsymbol{\rho}_S, \boldsymbol{\rho}_I) \propto \exp \left[-\frac{2}{\sigma_-^2 (1 + \lambda_I/\lambda_S)^2} |\boldsymbol{\rho}_S - \boldsymbol{\rho}_I|^2 \right], \quad (6b)$$

where $\sigma_+ = w_p$ with w_p being the pump waist and $\sigma_- = \sqrt{L\lambda_p\lambda_S/(2\pi\lambda_I)}$ with λ_p , λ_I and λ_S being the wavelengths of the pump, idler and signal photons, respectively, and L being the crystal length.

When the crystal is weakly pumped, the likelihood of multi-photon emission and stimulated emission is negligible compared to that of two-photon emissions [33, 34]. In this case, the quantum state of light created by the two sources is the linear superposition of two-photon states generated by each of them individually. It then follows from Eq. (3) that the resulting state is given by

$$|\psi\rangle = \int d\mathbf{k}_S d\mathbf{k}_I C(\mathbf{k}_S, \mathbf{k}_I) \times \left[\hat{a}_{S_1}^\dagger(\mathbf{k}_S) \hat{a}_{I_1}^\dagger(\mathbf{k}_I) + e^{i\phi_p} \hat{a}_{S_2}^\dagger(\mathbf{k}_S) \hat{a}_{I_2}^\dagger(\mathbf{k}_I) \right] |vac\rangle, \quad (7)$$

where the two passes of the pump through the crystal are labeled by 1 and 2, the quantity ϕ_p represents a phase, $\hat{a}_{S_j}^\dagger(\mathbf{k}_S) \hat{a}_{I_j}^\dagger(\mathbf{k}_I) |vac\rangle = |\mathbf{k}_S\rangle_{S_j} |\mathbf{k}_I\rangle_{I_j}$ ($j = 1, 2$) with \hat{a}^\dagger and $|vac\rangle$ representing a photon creation operator and the vacuum state, respectively. We have also assumed for simplicity that the sources emit with the same probability and dropped the normalization factor $1/\sqrt{2}$ because it is irrelevant to our analysis.

As mentioned in Sec. III, the idler beam, I_1 , emitted by Q_1 , is aligned with the idler beam I_2 that is emitted by Q_2 . An absorptive knife edge is placed in the idler beam between Q_1 and Q_2 . The idler photon is not detected. The signal photon is detected after aligning the signal beams through the source. In order to determine $\Delta(\mathbf{k}_I | \mathbf{k}_S)$ and $\Delta(\boldsymbol{\rho}_I | \boldsymbol{\rho}_S)$, we obtain expressions for the

interference patterns in the far-field and near-field [30] configurations, respectively. In the former case, both the knife edge and the camera are placed on the Fourier plane of the sources (Fig. 2a) while in the latter case, they are placed in the image plane of the sources (Fig. 2b).

Suppose that $\boldsymbol{\rho}_o \equiv (x_o, y_o)$ represents a point on the object plane. An absorptive knife edge placed along the x_o -axis (i.e., $y_o = 0$) is represented by the amplitude transmission coefficient

$$T(\boldsymbol{\rho}_o) = T(x_o, y_o) = \begin{cases} 0, & \text{if } x_o < 0, \\ 1, & \text{if } x_o \geq 0. \end{cases} \quad (8)$$

When the knife edge is inserted in the idler beam between the two sources, the relationships between the idler fields generated by Q_1 and Q_2 are given by the following two equations for the far-field (ff) and near-field (nf) cases, respectively [26, 27]:

$$\hat{a}_{I_2}(\mathbf{k}_I) = e^{i\phi_I} [F_{ff} T(\boldsymbol{\rho}_o) \hat{a}_{I_1}(\mathbf{k}_I) + R_{ff}(\boldsymbol{\rho}_o) \hat{a}_0(\mathbf{k}_I)], \quad (9a)$$

$$\hat{E}_{I_2}^{(+)}(\boldsymbol{\rho}_I) = e^{i\phi_I} [F_{nf} T(\boldsymbol{\rho}_o) \hat{E}_{I_1}^{(+)}(\boldsymbol{\rho}_I) + R_{nf}(\boldsymbol{\rho}_o) \hat{E}_0^{(+)}(\boldsymbol{\rho}_I)], \quad (9b)$$

where the phase ϕ_I is accumulated due to the propagation of the idler photon from Q_1 to Q_2 . In Eq. (9a), a photon with transverse momentum $\hbar\mathbf{k}_I$ impinges on the point $\boldsymbol{\rho}_o$, i.e., $\mathbf{k}_I = (2\pi/\lambda_I f) \boldsymbol{\rho}_o$ with f being the focal length of the positive lens placed in idler path and $0 \leq F_{ff} \leq 1$ characterizes losses of idler photons between the two sources due to misalignment and absorption/reflection at various optical components. When $F_{ff} = 0$, the idler photon is lost with 100% probability; and when $F_{ff} = 1$, no idler photon is lost. Such losses and the interaction of the object with idler photons can be quantum mechanically treated like a beam splitter with single input [15]; in Eq. (9a), \hat{a}_0 is the vacuum field at the unused port of the beam splitter (object) and the relation $R_{ff}(\boldsymbol{\rho}_o) = \sqrt{1 - [F_{ff} T(\boldsymbol{\rho}_o)]^2}$ ensures that the photon number is conserved. Likewise, in the near-field case [Eq. (9b)], we have $R_{nf}(\boldsymbol{\rho}_o) = \sqrt{1 - [F_{nf} T(\boldsymbol{\rho}_o)]^2}$ and $\hat{E}_0^{(+)}(\boldsymbol{\rho}_I)$ represents the vacuum field at the unused port of the beam splitter (object). In this case, $\hat{E}_{I_2}^{(+)}(\boldsymbol{\rho}_I) = \int d\mathbf{k}_{I_2} \hat{a}_{I_2}(\mathbf{k}_I) e^{i\mathbf{k}_{I_2} \cdot \boldsymbol{\rho}_I}$ represents the propagating part of the idler field at source Q_2 .

Using Eqs. (7), (9a), and (9b), we obtain the following

states for the far- and near-field cases:

$$\begin{aligned} |\psi\rangle_{ff} &= \int d\mathbf{k}_S d\mathbf{k}_I C(\mathbf{k}_S, \mathbf{k}_I) \left(|\mathbf{k}_S\rangle_{S_1} \right. \\ &\quad \left. + e^{i(\phi_p - \phi_I)} F_{ff} T^*(\boldsymbol{\rho}_o) |\mathbf{k}_S\rangle_{S_2} \right) |\mathbf{k}_I\rangle_{I_1} \\ &+ \int d\mathbf{k}_S d\mathbf{k}_I C(\mathbf{k}_S, \mathbf{k}_I) e^{i(\phi_p - \phi_I)} R_{ff}^*(\boldsymbol{\rho}_o) |\mathbf{k}_S\rangle_{S_2} |\mathbf{k}_I\rangle_{I_0}, \end{aligned} \quad (10a)$$

$$\begin{aligned} |\psi\rangle_{nf} &= \int d\mathbf{k}_{I_1} d\mathbf{k}_{S_1} C(\mathbf{k}_S, \mathbf{k}_I) e^{i(\phi_p - \phi_I)} |\mathbf{k}_{I_1}\rangle_{I_1} |\mathbf{k}_{S_1}\rangle_{S_1} \\ &+ \int d\mathbf{k}_{I_2} d\mathbf{k}_{S_2} d\mathbf{k}'_I C(\mathbf{k}_{I_2}, \mathbf{k}_{S_2}) e^{i(\phi_p - \phi_I)} |\mathbf{k}_{S_2}\rangle_{S_2} \\ &\otimes (F_{nf} \tilde{T}'^*(\mathbf{k}_{I_2} - \mathbf{k}'_I) |\mathbf{k}'_I\rangle_{I_1} + \tilde{R}'^*_{nf}(\mathbf{k}_{I_2} - \mathbf{k}'_I) |\mathbf{k}'_I\rangle_0), \end{aligned} \quad (10b)$$

where $\tilde{T}(\mathbf{k}_I)$ and $\tilde{R}(\mathbf{k}_I)$ are the Fourier transforms of $T(\boldsymbol{\rho}_o)$ and $R(\boldsymbol{\rho}_o)$, respectively; and we applied the convolution theorem to obtain Eq. (10b) as shown in [27].

The signal photon is detected after aligning the signal beams through the source. Consequently, the positive frequency part of the quantized electric field, at a point $\boldsymbol{\rho}_c \equiv (x_c, y_c)$ on the camera plane, in the far-field and near-field configurations, respectively, can be represented by [26, 27, 32]

$$\hat{E}_{ff}^{(+)}(\boldsymbol{\rho}_c) \propto \hat{a}_{S_1}(\mathbf{k}_S) + e^{i\phi_S} \hat{a}_{S_2}(\mathbf{k}_S), \quad (11a)$$

$$\hat{E}_{nf}^{(+)}(\boldsymbol{\rho}_c) \propto \int d\mathbf{k}_S [\hat{a}_{S_1}(\mathbf{k}_S) + e^{i\phi_S} \hat{a}_{S_2}(\mathbf{k}_S)] e^{i\mathbf{k}_S \cdot \boldsymbol{\rho}_S}, \quad (11b)$$

where ϕ_S is the phase accumulated due to the propagation of the signal photon from the crystal to the mirror (M2 in Fig. 2) and back to the crystal; in Eq. (11a) $\mathbf{k}_S = (2\pi/\lambda_S f_c) \boldsymbol{\rho}_c$ with f_c being the focal length of the positive lens placed in signal path; and in Eq. (11b), $\boldsymbol{\rho}_S = \boldsymbol{\rho}_c/M_S$ with M_S being the magnification of the imaging system that images the crystal on the camera along the signal path.

We can now determine the single-photon counting rate (intensity), $\mathcal{R}(\boldsymbol{\rho}_c)$, at a point $\boldsymbol{\rho}_c$ on the camera using the well-known formula introduced by Glauber [35]: $\mathcal{R}(\boldsymbol{\rho}_c) \propto \langle \psi | \hat{E}^{(-)}(\boldsymbol{\rho}_c) \hat{E}^{(+)}(\boldsymbol{\rho}_c) | \psi \rangle$, where $\hat{E}^{(-)} = \{\hat{E}^{(+)}\}^\dagger$. It follows from Eqs. (10a)–(11b), Eq. (8), and Eqs. (4) and (5) that the single-photon counting rates in the far-field and near-field configurations are, respectively, given by (Appendix B)

$$\begin{aligned} \mathcal{R}_{ff}(x_c, y_c) &\propto 1 + \frac{1}{2} F_{ff} \left(1 - \text{Erf} \left[\frac{\sqrt{2}\pi\sigma_+}{f_c\lambda_S} x_c \right] \right) \cos \phi_{in}, \end{aligned} \quad (12a)$$

$$\begin{aligned} \mathcal{R}_{nf}(x_c, y_c) &\propto 1 + \frac{1}{2} F_{nf} \left(1 + \text{Erf} \left[\frac{\sqrt{2}\lambda_S}{M_S(\lambda_I + \lambda_S)\sigma_-} x_c \right] \right) \cos \phi_{in}, \end{aligned} \quad (12b)$$

where $\phi_{in} = \phi_p - \phi_I - \phi_S$ is the tunable interferometric phase, $(x_c, y_c) \equiv \boldsymbol{\rho}_c$, and Erf represents the error function. It is evident that if ϕ_{in} is varied $\mathcal{R}_{ff}(\boldsymbol{\rho}_c)$ and $\mathcal{R}_{nf}(\boldsymbol{\rho}_c)$ vary sinusoidally. Therefore, Eqs. (12a) and (12b) represent interference patterns. We note that both \mathcal{R}_{ff} and \mathcal{R}_{nf} do not depend on y_c , which is expected because the knife edge was placed along x_o -axis on the object plane [see Eq. (8)].

If we now determine the visibility [36] of the two interference patterns given by Eqs. (12a) and (12b), we find that

$$\mathcal{V}_{ff}(x_c) = \frac{F_{ff}}{2} \left(1 - \text{Erf} \left[\frac{\sqrt{2}\pi\sigma_+}{f_c\lambda_S} x_c \right] \right), \quad (13a)$$

$$\mathcal{V}_{nf}(x_c) = \frac{F_{nf}}{2} \left(1 + \text{Erf} \left[\frac{\sqrt{2}\lambda_S}{M_S(\lambda_I + \lambda_S)\sigma_-} x_c \right] \right). \quad (13b)$$

It can be noted that these visibilities give images of the knife edge in the far-field and near-field configurations; that is, each represents the edge-spread function (ESF) in the respective configuration.

The visibilities (ESFs) given by Eqs. (13a) and (13b) can be used to measure the quantities σ_+ and σ_- . The spreads of these two ESFs (D_k and D_ρ) can be defined by the inverse of the coefficients that multiply x_c within the error function, i.e.,

$$\sigma_+ = \frac{f_c\lambda_S}{\sqrt{2}\pi} \frac{1}{D_k}, \quad (14a)$$

$$\sigma_- = \frac{\sqrt{2}\lambda_S}{M_S(\lambda_I + \lambda_S)} D_\rho, \quad (14b)$$

where we note again that $\sigma_+ = w_p$ and $\sigma_- = \sqrt{L\lambda_p\lambda_S/(2\pi\lambda_I)}$. From the definition of the error function, it follows that these spreads (D_k and D_ρ) are the distances for which the visibilities \mathcal{V}_{ff} and \mathcal{V}_{nf} rise from 24% to 76% of their maximum values. Therefore, D_k and D_ρ are experimentally measurable quantities, which are related to σ_+ and σ_- by Eqs. (14a) and (14b), respectively. That is, σ_+ and σ_- can be experimentally obtained from the visibility of the interference patterns. We now proceed to show how to verify the spatial (momentum-position) entanglement by testing both the EPR criterion and the MGVT criterion.

Testing the EPR criterion: One can show from the first principle that the conditional variances in Eq. (1) are related to σ_+ and σ_- by the following relations (Appendix C)

$$\Delta^2(k_{Ix}|k_{Sx}) \approx \frac{1}{\sigma_+^2}, \quad (15a)$$

$$\Delta^2(x_I|x_S) \approx \left[\frac{1 + (\lambda_I/\lambda_S)}{2} \right]^2 \sigma_-^2. \quad (15b)$$

Using Eqs. (14a), (14b), (15a) and (15b), the product of the conditional variances in the EPR-criterion [Eq. (1)]

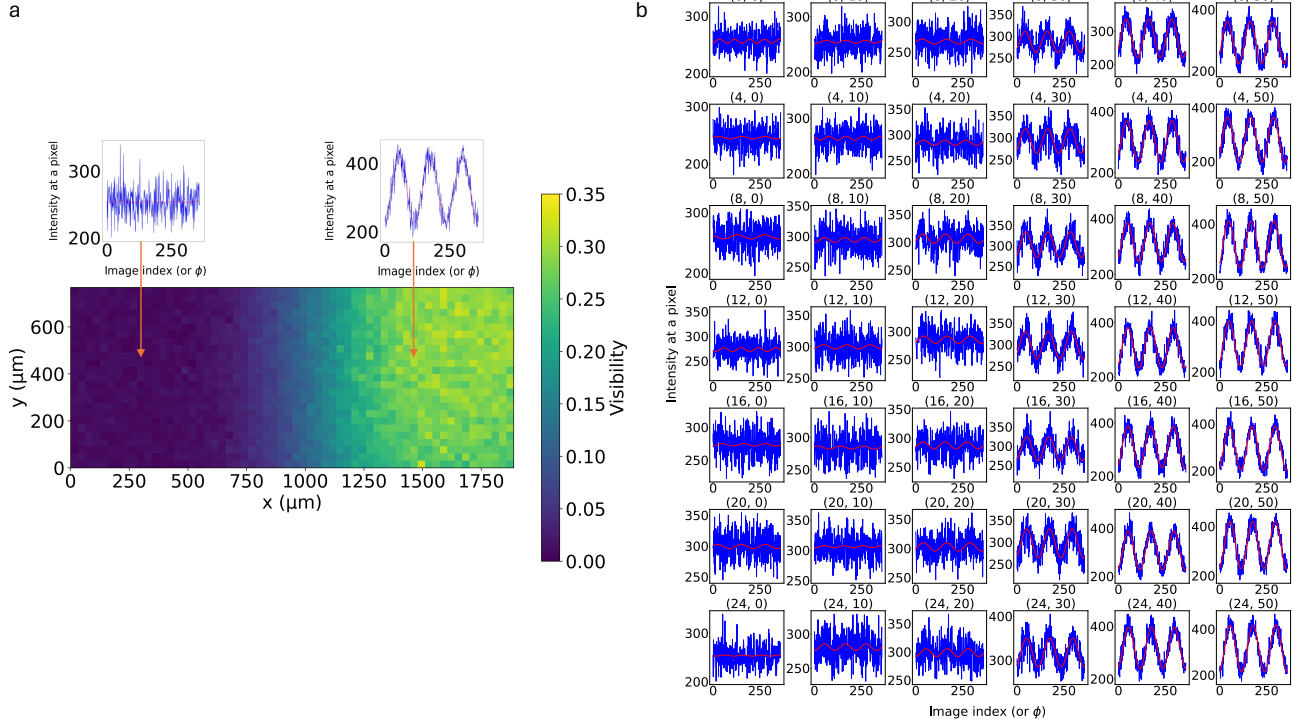


FIG. 3. Experimental results for momentum space. (a) Represents the reconstructed visibility map of the knife edge – an absorptive sharp object. (b) Illustration of the imaging process with the EMCCD camera capturing the detected beam intensity as the interferometric phase ϕ is scanned. The intensity varies with the phase change. By examining the recorded interference pattern on a pixel-by-pixel, independent information about each point on the object is derived. A sinusoidal function is fitted to the interference pattern of each pixel at various phases. This fitting process is demonstrated for a few pixels. The visibility for each pixel is determined from the obtained fit.

can be expressed as

$$\Delta^2(x|x_S) \Delta^2(k_{Ix}|k_{Sx}) = \frac{\pi^2}{f_c^2 \lambda_S^2 M_S^2} D_\rho^2 D_k^2. \quad (16)$$

In our method, the quantity on the right-hand side of Eq. (16) is determined from single-photon interference data. If this quantity is smaller than 1/4, the photon pair is spatially entangled according to the EPR criterion.

Testing the MGVT criterion: The quantities $\Delta^2 K_{x+}$ and $\Delta^2 X_-$ appearing in the MGVT criterion [Eq. (2)] can also be related to the experimentally measurable spreads of ESFs [see Appendix D, Eqs. (D3a) and (D3b)]. Using these relations, the product of the conditional variances in the MGVT criterion [Eq. (2)] can be expressed as

$$\Delta^2 K_{x+} \Delta^2 X_- = \frac{\pi^2}{f_c^2 \lambda_S^2 M_S^2} D_k^2 D_\rho^2. \quad (17)$$

Once again, the quantity on the right-hand side of Eq. (17) can be determined from single-photon interference data. If the value of this quantity is smaller than 1, the photon pair is spatially entangled according to the MGVT criterion.

We now briefly discuss the robustness of our method in the context of key experimental imperfections. The

factors F_{ff} and F_{nf} — which characterize losses of idler photons and misalignment of idler beams in the far-field and near-field configurations, respectively — appear in the single-photon counting rates given by Eqs. (12a) and (12b). It is evident from these equations that the visibility of the interference patterns will depend on these factors: a higher loss in the idler path (i.e., smaller F_{ff} and F_{nf}) results in a lower visibility of the signal interference patterns [Eqs. (13a) and (13b)]. However, it is remarkable that the values of σ_+ and σ_- obtained using these interference patterns do not depend on F_{ff} and F_{nf} as can be observed in Eqs. (14a) and (14b). Therefore, our method is applicable even when the interference-visibility is very low due to high loss of idler photons and/or idler beam misalignment. This fact is supported by the experimental results presented in the next section.

V. RESULTS

In order to analyze the position-momentum entanglement of signal and idler photons generated at the nonlinear crystal, without relying on coincidence detection, we captured intensity variations of the detected beams while varying the interferometric phase ϕ_{in} . We recorded

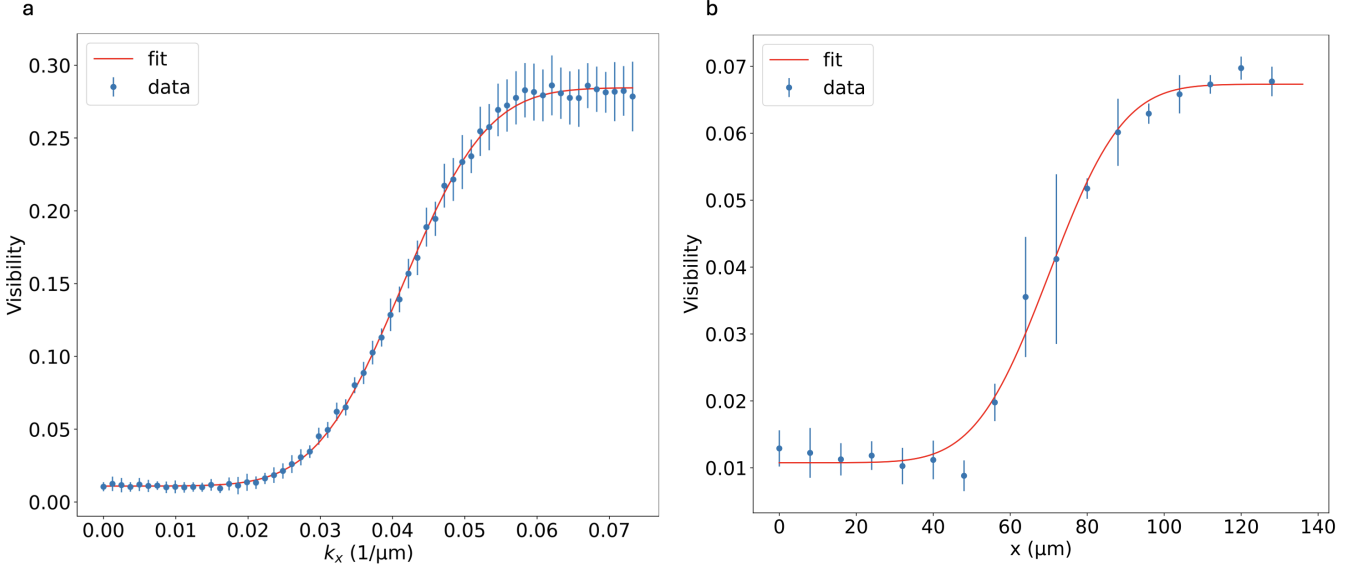


FIG. 4. Quantitative measurement of the edge-spread function in momentum and position space. (a) Cross-section of the reconstructed visibility image obtained from a sharp knife-edge placed in the momentum plane. The visibility profile is fitted with an error function, and the characteristic width D_k is extracted from the 76%–24% rise interval. The measured value is $D_k = (352 \pm 17) \mu\text{m}$, in good agreement with the theoretical prediction of $337 \mu\text{m}$. (b) Corresponding measurement in the position plane. From the error-function fit, we obtain $D_\rho = (28 \pm 3) \mu\text{m}$, compared with the theoretical value of $21 \mu\text{m}$. The reduced visibilities in both measurements reflect the significant losses present in the idler arm; nonetheless, the extracted widths D_k and D_ρ remain unaffected by these losses, demonstrating the robustness of the method.

a total of 360 frames, each associated with a value of $\phi_{in} = \phi_1, \phi_2, \dots, \phi_{360}$. Subsequently, we analyzed the recorded interference patterns on a pixel-by-pixel basis to form a visibility image (see Fig. 3).

In the case of imperfect momentum correlation, a single point on the camera no longer corresponds to just one point on the object due to the varying momenta of undetected photons. As momentum correlation weakens, the range broadens resulting in information from multiple points on the object appearing at a single point on the camera. This indicates that a weaker momentum correlation decreases the spatial resolution.

In order to evaluate the variance in the far field, we use the visibility image of the knife edge. From the cross-section of the position-dependent visibility image, we average over 20 pixel-rows (Fig. 3a) and fit it with the error function. The measured visibility with respect to distance in the momentum space is shown in Fig. 4a. Quantitatively, the spread of the ESF is given by the parameter D_k which is the characteristic distance, on the camera plane, over which the visibility rises from 24% to 76% of its maximum value (Fig. 4a). This experimentally measured value of D_k is $352 \pm 17 \mu\text{m}$, which is in good agreement with the corresponding theoretical value $D_k = 337 \mu\text{m}$. The theoretical value is obtained from Eq. (14a) by substituting the following values for the experimental parameters: $\sigma_+ = w_p = 108 \mu\text{m}$, $\lambda_S = 810 \text{ nm}$, and $f_c = 200 \text{ mm}$. Note that our method of measuring D_k , is an alternative to the method some of us introduced in Refs. [32, 37], which was limited to

the measurement of momentum correlations.

Similarly, to determine the variance in the near field (position correlation), the intensity data for each pixel was analyzed and the visibility was calculated. The visibility image of the knife edge is depicted in Fig. 4b. For position measurements, both the knife edge and the camera are on the image plane of the crystal. Based on the error function fit in Fig. 4b, D_ρ which is the 24%–76% width of the edge spread function, turns out to be $28 \pm 3 \mu\text{m}$. The theoretical value of D_ρ obtained using Eq. (14b) is $16 \mu\text{m}$; here $\sigma_- = \sqrt{L\lambda_p\lambda_S/(2\pi\lambda_I)}$ and the experimental parameters are $L = 2 \text{ mm}$, $\lambda_p = 405 \text{ nm}$, $\lambda_S = \lambda_I = 810 \text{ nm}$, and $M_s = 1$. This shows that the experimental value matches the theoretical value with good accuracy.

From the experimental results, i.e., measurements of D_ρ and D_k we calculate, using Eq. (16), the product of the conditional variances in momentum and position to be

$$\Delta^2(x_I|x_S) \Delta^2(k_{Ix}|k_{Sx}) = (3.30 \pm 0.75) \times 10^{-2} < \frac{1}{4}, \quad (18)$$

which shows a violation of the EPR criterion [Eq. (1)]. The corresponding theoretical value of the product of the conditional variances is $0.011 < 1/4$. This violation certifies the position-momentum entanglement of the signal and idler photons produced in the SPDC process.

To strengthen our results further, we have also verified the violation of the MGVT separability crite-

tion. The theoretical result is obtained by using Eqs. (D3a) and (D3b) of Appendix D, and is found to be $\Delta^2 K_{x+} \Delta^2 X_- = 0.011 < 1$. The experimental value of the product is obtained using the experimentally measured values of D_k and D_ρ . It is given by $\Delta^2 K_{x+} \Delta^2 X_- = (3.30 \pm 0.75) \times 10^{-2} < 1$, which demonstrates the violation of the MGVT criterion.

The measured product of conditional variances in both position and momentum spaces are in good agreement with the corresponding theoretical values. The small difference is due to experimental limitations, especially due to imperfections in the distances used in the imaging system, non-negligible lens thickness, imperfect positioning of knife edge, and relatively large camera pixel size. These affect more prominently the results for near-field correlations.

VI. DISCUSSION

Our method is highly resistant to key experimental imperfections. Dominating imperfections in our experiment are loss of idler photons at various optical components and misalignment of idler beams. These imperfections reduce the visibility of single-photon interference patterns and cannot be compensated for in any way. We have provided a theoretical justification at the end of Sec. IV explaining why our method is resistant to such experimental imperfections. Our experimental data confirm significant presence of these imperfections during the experiment: the maximum value of the visibility in the far-field configuration is less than 0.3 (Fig. 4a) and that in the near-field configuration is less than 0.07 (Fig. 4b). Despite the presence of such high level of experimental imperfections, our method has worked remarkably well.

Our technique is fundamentally different from the one used in [38] where EPR correlations in a bi-photon system have been studied with only single-photon detection. Unlike [38], we do not measure the cross-spectral density, nor do we construct the conditional probability densities to measure the variances. Instead, we determine the variances directly from the visibility data.

We consider a two-photon pure state in our investigation to certify spatial entanglement in the system. However, it should be possible to extend the analysis to verify mixed state continuous variable entanglement using our method. This interferometric technique with undetected photons has been used to characterize mixed state entanglement in discrete variables (i.e., polarization degree of freedom) [17–20].

VII. SUMMARY

We have demonstrated both theoretically and experimentally that using an interferometric technique, it is possible to verify entanglement in an infinite-dimensional

bipartite photonic system simply without any coincidence measurement or postselection. From the visibility data obtained from single-photon interference patterns, we have been able to study the EPR correlations and demonstrate the violation of the MGVT criterion. Our investigation yields good agreement between the theoretical values and the experimentally measured results. Furthermore, since our method does not involve any coincidence detection, it is naturally well suited to study entanglement in highly non-degenerate sources, particularly when suitable detectors are not available for one of the wavelengths.

AUTHOR CONTRIBUTION

M.L. conceived the idea of the project, supervised the theoretical part of the project, and discussed the results. S.K. built and implemented the experimental setup, performed all measurements, developed the data analysis software, and carried out the full experimental data analysis. B.V. carried out the theoretical analysis and discussed the results. R.L. designed the setup, discussed the results and supervised the experimental part of the project. G.B.L. discussed the implementation, results, and advised S.K. throughout the entire experimental implementation, including the setup, the alignment and the data collection. P.S. reviewed the data analysis and discussed the results. B.V., S.K. and M.L. wrote the manuscript with contributions of all the authors.

ACKNOWLEDGMENTS

We thank Inna Kviatkovsky for fruitful discussions about the quantum imaging setup. This material is based upon work supported by the Air Force Office of Scientific Research under award number FA9550-23-1-0216. S.K., P.S., and R.L. acknowledge the support of the following funding agencies: Foundation for Polish Science (FIRST TEAM project FENG.02.02-IP.05-0253/23); Narodowe Centrum Nauki (grant 2022/47/B/ST7/03465); National Centre for Research and Development QuantERA II projects: QM3 (QuantERAII/02/QM3/03/2024) and EXTRASENS (QuantERAII/02/EXTRASENS/02/2024); HORIZON EUROPE Marie Skłodowska-Curie Actions (FLORIN ID 101086142).

Appendix A: Probability distributions corresponding to twin-photon momentum and position correlations generated by SPDC

The joint probability distribution of the twin photons, produced in degenerate SPDC [31, 39], with the double Gaussian approximation, can be generalized to the non-degenerate case. In the momentum space, the joint

probability density is written as

$$P(\mathbf{k}_S, \mathbf{k}_I) = \frac{\sigma_+^2 \sigma_-^2}{4\pi^2} \left(1 + \frac{\lambda_I}{\lambda_S}\right)^2 \exp\left[-\frac{\sigma_+^2}{2} |\mathbf{k}_I + \mathbf{k}_S|^2\right] \times \exp\left[-\frac{\sigma_-^2}{2} \left|\mathbf{k}_S - \frac{\lambda_I}{\lambda_S} \mathbf{k}_I\right|^2\right], \quad (\text{A1})$$

where $\sigma_+ = w_p$ with w_p being the pump waist and $\sigma_- = \sqrt{L\lambda_p\lambda_S/(2\pi\lambda_I)}$ with λ_p , λ_I and λ_S being the wavelengths of the pump, idler and signal photons, respectively, and L being the crystal length. For the typical values of parameters in experiments, the second exponent in Eq. (A1) varies very slowly compared to the first exponent. It is customary to treat the second exponent as a constant. Therefore, in the far-field scenario, we can reduce Eq. (A1) to

$$P(\mathbf{k}_S, \mathbf{k}_I) \propto \exp\left[-\frac{\sigma_+^2}{2} |\mathbf{k}_I + \mathbf{k}_S|^2\right], \quad (\text{A2})$$

which is Eq. (6a) in the main text.

The joint probability distribution of the twin photons in the position space is written as

$$P(\boldsymbol{\rho}_S, \boldsymbol{\rho}_I) = \left(\frac{4}{\pi^2 \sigma_+^2 \sigma_-^2 (1 + \lambda_I/\lambda_S)^2}\right) \times \exp\left[-\frac{2}{\sigma_+^2 (1 + \lambda_I/\lambda_S)^2} |\boldsymbol{\rho}_I + (\lambda_I/\lambda_S) \boldsymbol{\rho}_S|^2\right] \times \exp\left[-\frac{2}{\sigma_-^2 (1 + \lambda_I/\lambda_S)^2} |\boldsymbol{\rho}_S - \boldsymbol{\rho}_I|^2\right]. \quad (\text{A3})$$

For typical experimental parameters, the first exponent in Eq. (A3) varies very slowly compared to the second one. Because of this, we can treat the first exponent as a constant and approximate Eq. (A3) by

$$P(\boldsymbol{\rho}_S, \boldsymbol{\rho}_I) \propto \exp\left[-\frac{2}{\sigma_-^2 (1 + \lambda_I/\lambda_S)^2} |\boldsymbol{\rho}_S - \boldsymbol{\rho}_I|^2\right], \quad (\text{A4})$$

which is Eq. (6b) in the main text.

Appendix B: Derivations of Eqs. (12a) and (12b)

We first present the derivation of Eq. (12a), which gives an expression of the single-photon counting rate at the camera obtained in the far-field case. In this case, the single-photon counting rate is given by [35] $\mathcal{R}_{ff}(\boldsymbol{\rho}_c) \propto \int d\mathbf{k}_I P(\mathbf{k}_S, \mathbf{k}_I) (1 + F_{ff} |T(\boldsymbol{\rho}_o)| \cos \phi_{in})$, where $\hat{E}_{ff}^{(-)} = \{\hat{E}_{ff}^{(+)}\}^\dagger$. Substituting for $|\psi\rangle_{ff}$ and $\hat{E}_{ff}^{(+)}$ from Eqs. (10a) and (11a), respectively, we find that

$$\mathcal{R}_{ff}(\boldsymbol{\rho}_c) \propto \int d\mathbf{k}_I P(\mathbf{k}_S, \mathbf{k}_I) (1 + F_{ff} |T(\boldsymbol{\rho}_o)| \cos \phi_{in}). \quad (\text{B1})$$

Now substituting for $T(\boldsymbol{\rho}_o)$ and $P(\mathbf{k}_S, \mathbf{k}_I)$ from Eqs. (8) and (A2) into Eq. (B1), we obtain Eq. (12a) in the main text:

$$\mathcal{R}_{ff}(x_c, y_c) \propto 1 + \frac{1}{2} F_{ff} \left(1 - \text{Erf}\left[\frac{\sqrt{2}\pi\sigma_+}{f_c\lambda_S} x_c\right]\right) \cos \phi_{in}, \quad (\text{B2})$$

where $(x_c, y_c) \equiv \boldsymbol{\rho}_c$.

We now show the derivation of Eq. (12b), which gives an expression for the single-photon counting rate at the camera obtained in the near-field case. In this case, the single-photon counting rate is given by $\mathcal{R}_{nf}(\boldsymbol{\rho}_c) \propto \int d\mathbf{k}_I P(\mathbf{k}_S, \mathbf{k}_I) (1 + F_{nf} |T(\boldsymbol{\rho}_o)| \cos \phi_{in})$, where $\hat{E}_{nf}^{(-)} = \{\hat{E}_{nf}^{(+)}\}^\dagger$. Substituting for $|\psi\rangle_{nf}$ and $\hat{E}_{nf}^{(+)}$ from Eqs. (10b) and (11b), respectively, we find that

$$\mathcal{R}_{nf}(\boldsymbol{\rho}_c) \propto \int d\boldsymbol{\rho}_o P(\boldsymbol{\rho}_c, \boldsymbol{\rho}_o) (1 + F_{nf} |T(\boldsymbol{\rho}_o)| \cos \phi_{in}), \quad (\text{B3})$$

where $\boldsymbol{\rho}_c = M_S \boldsymbol{\rho}_S$ and $\boldsymbol{\rho}_o = M_I \boldsymbol{\rho}_I$ with M_S being the magnification of the imaging system that images the crystal on the camera along the signal path and M_I being the magnification of the imaging system that images the crystal on the knife edge along the idler path. Now using expressions for $P(\boldsymbol{\rho}_c, \boldsymbol{\rho}_o)$ [Eq. (A4)] and $T(\boldsymbol{\rho}_o)$ [Eq. (8)] we obtain the following relation from Eq. (B3):

$$\mathcal{R}_{nf}(x_c, y_c) \propto 1 + \frac{1}{2} F_{nf} \left(1 + \text{Erf}\left[\frac{\sqrt{2}\lambda_S}{M_S(\lambda_I + \lambda_S)\sigma_-} x_c\right]\right) \cos \phi_{in}, \quad (\text{B4})$$

which is Eq. (12b) in the main text.

Appendix C: Derivations of Eqs. (15a) and (15b)

For a two-photon system, the conditional variance in both momentum and position is given by [6]

$$\Delta^2(k_{Ij}|k_{Sj}) = \int k_{Ij}^2 P(k_{Ij}|k_{Sj}) dk_{Ij} - \left(\int k_{Ij} P(k_{Ij}|k_{Sj}) dk_{Ij}\right)^2, \quad (\text{C1a})$$

$$\Delta^2(\rho_{Ij}|\rho_{Sj}) = \int \rho_{Ij}^2 P(\rho_{Ij}|\rho_{Sj}) d\rho_{Ij} - \left(\int \rho_{Ij} P(\rho_{Ij}|\rho_{Sj}) d\rho_{Ij}\right)^2, \quad (\text{C1b})$$

where $j = x, y$.

The conditional probability density, $P(\mathbf{k}_I|\mathbf{k}_S)$, can be obtained from the joint probability distribution Eq. (A1) using the standard formula: $P(\mathbf{k}_I|\mathbf{k}_S) =$

$P(\mathbf{k}_I, \mathbf{k}_S)/P(\mathbf{k}_S)$ which gives

$$\begin{aligned} P(\mathbf{k}_I|\mathbf{k}_S) &= \frac{1}{2\pi} \left[\sigma_+^2 + \left(\frac{\lambda_I}{\lambda_S} \right)^2 \sigma_-^2 \right] \\ &\times \exp \left[-\frac{1}{2} \frac{(\sigma_+^2 - (\lambda_I/\lambda_S)\sigma_-^2)^2}{\sigma_+^2 + (\lambda_I/\lambda_S)^2\sigma_-^2} |\mathbf{k}_S|^2 \right] \\ &\times \exp \left[-\frac{1}{2} (\sigma_+^2 + (\lambda_I/\lambda_S)^2\sigma_-^2) |\mathbf{k}_I|^2 \right] \\ &\times \exp \left[-(\sigma_+^2 - (\lambda_I/\lambda_S)\sigma_-^2)(\mathbf{k}_I \cdot \mathbf{k}_S) \right]. \end{aligned} \quad (\text{C2})$$

The conditional variance in momentum is formally determined using Eqs. (C1a) and (C2). It is found to be given by

$$\Delta^2(k_{I_j}|k_{S_j}) = \frac{1}{\sigma_+^2 + (\lambda_I/\lambda_S)^2\sigma_-^2}. \quad (\text{C3})$$

For typical values of the parameters in experiments, it turns out that $\sigma_+^2 + (\lambda_I/\lambda_S)^2\sigma_-^2 \approx \sigma_+^2$. Thus, Eq. (C3) can be expressed in the approximated form

$$\Delta^2(k_{I_j}|k_{S_j}) \approx \frac{1}{\sigma_+^2}. \quad (\text{C4})$$

By setting $j = x$ in Eq. (C4), we obtain Eq. (15a) in the main text.

We now derive Eq. (15b). The conditional probability density, $P(\boldsymbol{\rho}_I|\boldsymbol{\rho}_S)$, can be obtained from the joint probability distribution Eq. (A3) using the standard formula: $P(\boldsymbol{\rho}_I|\boldsymbol{\rho}_S) = P(\boldsymbol{\rho}_I, \boldsymbol{\rho}_S)/P(\boldsymbol{\rho}_S)$ which gives

$$\begin{aligned} P(\boldsymbol{\rho}_I|\boldsymbol{\rho}_S) &= \frac{2}{\pi} \left(\frac{1}{1 + (\lambda_I/\lambda_S)} \right)^2 \left(\frac{\sigma_+^2 + \sigma_-^2}{\sigma_+^2\sigma_-^2} \right) \\ &\times \exp \left[-\frac{2}{(1 + \lambda_I/\lambda_S)^2} \frac{(\sigma_+^2 - (\lambda_I/\lambda_S)\sigma_-^2)^2}{\sigma_+^2\sigma_-^2(\sigma_+^2 + \sigma_-^2)} |\boldsymbol{\rho}_S|^2 \right] \\ &\times \exp \left[-\frac{2}{(1 + \lambda_I/\lambda_S)^2} \left(\frac{1}{\sigma_+^2} + \frac{1}{\sigma_-^2} \right) |\boldsymbol{\rho}_I|^2 \right] \\ &\times \exp \left[-\frac{4}{(1 + \lambda_I/\lambda_S)^2} \right. \\ &\quad \left. \times \left(\frac{(\lambda_I/\lambda_S)}{\sigma_+^2} + \frac{1}{\sigma_-^2} \right) (\boldsymbol{\rho}_I \cdot \boldsymbol{\rho}_S) \right]. \end{aligned} \quad (\text{C5})$$

The conditional variance in the position space is obtained

using Eqs. (C1b) and (C5). It is given by

$$\Delta^2(\rho_{I_j}|\rho_{S_j}) = \left[\frac{1 + (\lambda_I/\lambda_S)}{2} \right]^2 \left(\frac{\sigma_+^2\sigma_-^2}{\sigma_+^2 + \sigma_-^2} \right). \quad (\text{C6})$$

Using the same approximation that we used to simplify the conditional variance in momentum [see the discussion below Eq. (C3)], we reduce Eq. (C6) to

$$\Delta^2(\rho_{I_j}|\rho_{S_j}) \approx \left[\frac{1 + (\lambda_I/\lambda_S)}{2} \right]^2 \sigma_-^2 \quad (\text{C7})$$

By setting $j = x$ in Eq. (C7), we obtain Eq. (15b) of the main text.

Appendix D: Derivation of Eq. (17)

In our case, the MGVT criterion (Eq. (2) in the main text) takes the form

$$\Delta^2 K_{x+} \Delta^2 X_- \geq 1, \quad (\text{D1})$$

where $K_{x+} = K_{Ix} + K_{Sx}$, $X_- = x_S - x_I$, and

$$\begin{aligned} \Delta^2 K_{x+} &= \int (K_{x+})^2 P(k_{Sx}, k_{Ix}) dk_{Ix} \\ &\quad - \left(\int K_{x+} P(k_{Sx}, k_{Ix}) dk_{Ix} \right)^2, \end{aligned} \quad (\text{D2a})$$

$$\begin{aligned} \Delta^2 X_- &= \int (X_-)^2 P(x_S, x_I) dx_I \\ &\quad - \left(\int X_- P(x_S, x_I) dx_I \right)^2, \end{aligned} \quad (\text{D2b})$$

with $P(k_{Ix}, k_{Sx})$ and $P(x_S, x_I)$ given by Eqs. (A1) and (A3), respectively. Carrying out these integrations, we obtain

$$\Delta^2 K_{x+} = \frac{2\pi^2}{f_c^2 \lambda_S^2} D_k^2 \quad (\text{D3a})$$

$$\Delta^2 X_- = \frac{1}{2M_S^2} D_\rho^2, \quad (\text{D3b})$$

where we applied Eqs. (14a) and (14b) from the main text and used the relations $\sigma_+ = w_p$ and $\sigma_- = \sqrt{L\lambda_p\lambda_S/(2\pi\lambda_I)}$.

Using Eqs. (D3a) and (D3b), we find that the left-hand side of Eq. (D1) is given by

$$\Delta^2 K_+ \Delta^2 X_- = \frac{\pi^2}{f_c^2 \lambda_S^2 M_S^2} D_k^2 D_\rho^2, \quad (\text{D4})$$

which is Eq. (17) in the main text.

[1] S. P. Walborn, C. Monken, S. Pádua, and P. S. Ribeiro, Spatial correlations in parametric down-conversion, *Physics Reports* **495**, 87 (2010).

[2] H. Defienne, W. Bowen, M. Chekhova, G. Barreto Lemos, D. Oron, S. Ramelow, N. Treps, and D. Faccio, Advances in quantum imaging, *Nature Photonics* (2024).

[3] D. Triggiani and V. Tamma, Estimation with ultimate quantum precision of the transverse displacement between two photons via two-photon interference sampling measurements, *Physical Review Letters* **132**, 180802 (2024).

[4] D. Triggiani and V. Tamma, Momentum-entangled two-photon interference for quantum-limited transverse-displacement estimation, *Physical Review A* **111**, 032605 (2025).

[5] M. Almeida, S. Walborn, and P. Souto Ribeiro, Experimental investigation of quantum key distribution with position and momentum of photon pairs, *Physical Review A—Atomic, Molecular, and Optical Physics* **72**, 022313 (2005).

[6] J. C. Howell, R. S. Bennink, S. J. Bentley, and R. W. Boyd, Realization of the einstein-podolsky-rosen paradox using momentum-and position-entangled photons from spontaneous parametric down conversion, *Physical Review Letters* **92**, 210403 (2004).

[7] R. S. Aspden, D. S. Tasca, R. W. Boyd, and M. J. Padgett, Epr-based ghost imaging using a single-photon-sensitive camera, *New Journal of Physics* **15**, 073032 (2013).

[8] P.-A. Moreau, F. Devaux, and E. Lantz, Einstein-podolsky-rosen paradox in twin images, *Physical review letters* **113**, 160401 (2014).

[9] M. Hor-Meyll, J. O. de Almeida, G. B. Lemos, P. H. S. Ribeiro, and S. P. Walborn, Ancilla-assisted measurement of photonic spatial correlations and entanglement, *Phys. Rev. Lett.* **112**, 053602 (2014).

[10] S. J. Freedman and J. F. Clauser, Experimental test of local hidden-variable theories, *Phys. Rev. Lett.* **28**, 938 (1972).

[11] A. Aspect, P. Grangier, and G. Roger, Experimental realization of einstein-podolsky-rosen-bohm gedankenexperiment: A new violation of bell's inequalities, *Phys. Rev. Lett.* **49**, 91 (1982).

[12] Z. Y. Ou, S. F. Pereira, H. J. Kimble, and K. C. Peng, Realization of the einstein-podolsky-rosen paradox for continuous variables, *Phys. Rev. Lett.* **68**, 3663 (1992).

[13] D. F. V. James, P. G. Kwiat, W. J. Munro, and A. G. White, Measurement of qubits, *Phys. Rev. A* **64**, 052312 (2001).

[14] M. Giustina, M. A. M. Versteegh, S. Wengerowsky, J. Handsteiner, A. Hochrainer, K. Phelan, F. Steinlechner, J. Kofler, J.-A. Larsson, C. Abellán, W. Amaya, V. Pruneri, M. W. Mitchell, J. Beyer, T. Gerrits, A. E. Lita, L. K. Shalm, S. W. Nam, T. Scheidl, R. Ursin, B. Wittmann, and A. Zeilinger, Significant-loophole-free test of bell's theorem with entangled photons, *Phys. Rev. Lett.* **115**, 250401 (2015).

[15] X. Zou, L. J. Wang, and L. Mandel, Induced coherence and indistinguishability in optical interference, *Physical review letters* **67**, 318 (1991).

[16] L. J. Wang, X. Y. Zou, and L. Mandel, Induced coherence without induced emission, *Phys. Rev. A* **44**, 4614 (1991).

[17] M. Lahiri, R. Lapkiewicz, A. Hochrainer, G. B. Lemos, and A. Zeilinger, Characterizing mixed-state entanglement through single-photon interference, *Physical Review A* **104**, 013704 (2021).

[18] G. B. Lemos, R. Lapkiewicz, A. Hochrainer, M. Lahiri, and A. Zeilinger, One-photon measurement of two-photon entanglement, *Physical Review Letters* **130**, 090202 (2023).

[19] S. Rajeev and M. Lahiri, Single-qubit measurement of two-qubit entanglement in generalized werner states, *Physical Review A* **108**, 052410 (2023).

[20] S. Rajeev and M. Lahiri, Complete measurement of two-photon density matrix by single-photon detection, arXiv preprint arXiv:2503.07999 (2025).

[21] M. Reid, Demonstration of the einstein-podolsky-rosen paradox using nondegenerate parametric amplification, *Physical Review A* **40**, 913 (1989).

[22] M. Reid, P. Drummond, W. Bowen, E. G. Cavalcanti, P. K. Lam, H. Bachor, U. L. Andersen, and G. Leuchs, Colloquium: the einstein-podolsky-rosen paradox: from concepts to applications, *Reviews of Modern Physics* **81**, 1727 (2009).

[23] M. P. Edgar, D. S. Tasca, F. Izdebski, R. E. Warburton, J. Leach, M. Agnew, G. S. Buller, R. W. Boyd, and M. J. Padgett, Imaging high-dimensional spatial entanglement with a camera, *Nature communications* **3**, 1 (2012).

[24] T. Herzog, J. Rarity, H. Weinfurter, and A. Zeilinger, Frustrated two-photon creation via interference, *Physical review letters* **72**, 629 (1994).

[25] G. B. Lemos, V. Borish, G. D. Cole, S. Ramelow, R. Lapkiewicz, and A. Zeilinger, Quantum imaging with undetected photons, *Nature* **512**, 409 (2014).

[26] M. Lahiri, R. Lapkiewicz, G. B. Lemos, and A. Zeilinger, Theory of quantum imaging with undetected photons, *Physical Review A* **92**, 013832 (2015).

[27] B. Viswanathan, G. B. Lemos, and M. Lahiri, Position correlation enabled quantum imaging with undetected photons, *Opt. Lett.* **46**, 3496 (2021).

[28] I. Kviatkovsky, H. M. Chrzanowski, and S. Ramelow, Mid-infrared microscopy via position correlations of undetected photons, *Optics Express* **30**, 5916 (2022).

[29] S. Mancini, V. Giovannetti, D. Vitali, and P. Tombesi, Entangling macroscopic oscillators exploiting radiation pressure, *Phys. Rev. Lett.* **88**, 120401 (2002).

[30] (), the term “near-field” is not to be confused with the one used in conventional near-field optics, because evanescent fields play no role in our case.

[31] D. Tasca, S. Walborn, P. S. Ribeiro, F. Toscano, and P. Pellat-Finet, Propagation of transverse intensity correlations of a two-photon state, *Physical Review A* **79**, 033801 (2009).

[32] M. Lahiri, A. Hochrainer, R. Lapkiewicz, G. B. Lemos, and A. Zeilinger, Twin-photon correlations in single-photon interference, *Physical Review A* **96**, 013822 (2017).

[33] H. Wiseman and K. Mølmer, Induced coherence with and without induced emission, *Physics Letters A* **270**, 245 (2000).

[34] M. Lahiri, A. Hochrainer, R. Lapkiewicz, G. B. Lemos, and A. Zeilinger, Nonclassicality of induced coherence without induced emission, *Physical Review A* **100**, 053839 (2019).

[35] R. J. Glauber, The quantum theory of optical coherence, *Physical Review* **130**, 2529 (1963).

[36] (), the visibility is given by the formula $(\mathcal{R}_{\max} - \mathcal{R}_{\min})/(\mathcal{R}_{\max} + \mathcal{R}_{\min})$.

[37] A. Hochrainer, M. Lahiri, R. Lapkiewicz, G. B. Lemos, and A. Zeilinger, Quantifying the momentum correlation between two light beams by detecting one, *Proceedings of the National Academy of Sciences* **114**, 1508 (2017).

[38] A. Bhattacharjee, N. Meher, and A. K. Jha, Measurement of two-photon position-momentum einstein-

podolsky–rosen correlations through single-photon intensity measurements, *New Journal of Physics* **24**, 053033 (2022).

[39] J. Schneeloch and J. C. Howell, Introduction to the transverse spatial correlations in spontaneous parametric down-conversion through the biphoton birth zone, *Journal of Optics* **18**, 053501 (2016).